IEEE Access
Multidisciplinary ⋮ Rapid Review ⋮ Open Access Journal

Received 8 April 2025, accepted 22 April 2025, date of publication 1 May 2025, date of current version 14 May 2025.

Digital Object Identifier 10.1109/ACCESS.2025.3566252

RESEARCH ARTICLE

Deep Learning-Driven Beam-Steering for Dual-Polarized 28 GHz Antenna Arrays in 5G Wireless Networks

SITI ZAINAB M. HAMZAH[1], (Member, IEEE),
NORUN FARIHAH ABDUL MALEK[1], (Senior Member, IEEE),
SARAH YASMIN MOHAMAD[1], (Senior Member, IEEE),
FARAH NADIA MOHD ISA[1], (Senior Member, IEEE),
TEDDY SURYA GUNAWAN[1], (Senior Member, IEEE),
AND KUO-SHENG CHIN[2], (Senior Member, IEEE)

[1]Department of Electrical and Computer Engineering, International Islamic University Malaysia, Jalan Gombak, Kuala Lumpur 53100, Malaysia
[2]Department of Electronic Engineering, Chang Gung University, Guishan District, Taoyuan 333, Taiwan

Corresponding author: Norun Farihah Abdul Malek (norun@iium.edu.my)

This work was supported in part by the Ministry of Higher Education, Malaysia, under Grant FRGS/1/2024/TK08/UIAM/02/1.

ABSTRACT This study explores the development of a 28 GHz array antenna with beam-steering capability, consisting of four elements with dual linear polarization at ±45 degrees. We propose a method for synthesizing the array antenna's radiation pattern using an active element pattern-deep neural network (AEP-DNN). Beam-steering has become an attractive feature for researchers, as it enables users to move freely without affecting signal strength. An array analysis was conducted using a feedforward deep neural network (DNN) to generate a radiation pattern that achieves the desired steering angles. The proposed method takes radiation patterns as inputs and outputs the corresponding phase values for the antenna elements. The training dataset for the array antenna consisted of 6,859 radiation patterns, generated by adjusting the antenna element phases, which were then used to train the DNN model with minimal complexity. The radiation pattern was computed using AEP method since it is faster and less complex compared to full-wave modelling methods. The DNN model was initially tested using radiation patterns from an ideal square shape. After training, the model was evaluated by inserting desired beam-steering angles of 5 and 10 degrees, and it was found that the radiation pattern produced by the DNN closely matched the intended input pattern. The DNN learning process takes approximately 2 to 3 minutes in terms of processing time. The training and validation Root Mean Square Error (RMSE) and loss values converge to a minimum range of 1.3 to 2.3. Furthermore, the AEP-DNN method was successfully validated using the pattern multiplication method, full-wave modelling, and measurement methods to verify the feasibility and reliability of the training and validation data, as well as the resulting radiation pattern. This antenna, incorporating AEP-DNN technology, holds significant potential for various applications, particularly in mobile communications.

INDEX TERMS Dual-polarized antenna arrays, millimeter-waves, beam-steering, 28 GHz frequency, active element pattern, deep neural network, 5G wireless communication.

I. INTRODUCTION

The expected advantages of 5G include enhanced economic development, education, employment, transportation, power networks, healthcare facilities, various industries, and more, significantly improving our daily lives [1]. Relying on 4G is no longer sufficient for tasks such as streaming videos on YouTube or storing data in the cloud, creating a demand for 5G services. While 2G was designed primarily for voice communication, 3G introduced both voice calls and data

The associate editor coordinating the review of this manuscript and approving it for publication was Bilal Khawaja.

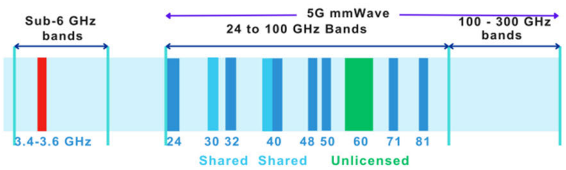

FIGURE 1. Frequency bands for millimeter waves.

usage, and 4G enabled fast internet browsing, 5G is the first technology that supports widespread computing capabilities for the Internet of Things (IoT). 5G wireless technologies offer significant benefits, including reduced latency (in the millisecond range), data transfer speeds of up to 10 Gbps, and the ability to connect 100 billion wireless devices [2]. Fig. 1 illustrates possible frequency bands of millimetre waves.

To achieve the maximum potential data rate for 5G, expanding the bandwidth of beams is crucial. This research addresses this challenge by utilizing higher frequencies, such as 28 GHz. However, millimeter-wave frequencies are known for their high free-space loss and penetration loss, which can be mitigated using high-gain antennas. A high-gain antenna can help reduce these losses [3]. However, narrow beams may limit the propagation of millimeter-wave multipath components, highlighting the importance of beam-steering capabilities in phased array antennas.

Recent research has focused extensively on developing reliable millimeter-wave antennas for wireless communication systems. For instance, a study [4] demonstrates the potential of small antennas for use in millimeter-wave applications, particularly at 28 GHz. This design measures 16 $\times$ 39 mm^2 and operates within the frequency range of 27.089 to 28.856 GHz. A tree-shaped design, tilted at a 30° angle, enhances the gain and reduces the antenna size, achieving a 9.04 dBi gain and 76.01% radiation efficiency when arranged in a linear formation with a single feeding port. Earlier research by [5] describes what was initially thought to be a flat array but is a linear array antenna with 16 elements fed in series. This design is well-suited for modern technologies such as massive MIMO and millimeter-wave communication, supporting data rates of up to 10 Gbps. The 1 $\times$ 16-element antenna array uses tapered microstrip lines and bending lines, resulting in a gain of 17.9 dBi and a bandwidth of 1 GHz. The twisted transmission lines among the patch antenna components improve gain, return loss, bandwidth, and radiation efficiency.

5G also offers significant advantages in providing broader coverage compared to 4G, which is limited by beam coverage. The use of polarization diversity techniques, such as Dual Polarization Arrays (DPAs), can significantly improve signal coverage. DPAs are ideal for meeting the demands of 5G. However, the rapid expansion of wireless technology has introduced new requirements for DPAs, such as higher bandwidth, better isolation, and lower back lobe levels [6]. One common method to incorporate dual polarization into an antenna is through a stacked antenna technique. In [7], capacitive coupling feeding is used to operate a dual-polarized, dual-band antenna with three stacked patches. This configuration generates both vertical and horizontal signals through the feed, achieving a simulated gain exceeding 8.5 dBi in the 27.48-28.50 GHz band.

Additionally, proximity-feeding techniques have been applied to achieve dual-polarization capabilities. Reference [7], reports on a stacked patch antenna with dual bands and dual polarization, designed for 5G smartphones operating at 28 GHz and 39 GHz, with a simulated gain ranging from 11 to 12 dBi.

Another design [8] integrates a Ka-band folded transmit-array antenna with an X-band Fabry-Perot cavity antenna to enable dual polarization, achieving a 2.5 GHz bandwidth and a 23.6 dBi gain. Further developments in substrate-integrated cavity antennas also provide dual polarization capabilities. For example, [9], describes a substrate-integrated cavity for a stacked patch antenna with 8 elements and 12 PCB layers, resulting in a simulated bandwidth of 4 GHz and a gain of 16.5 dBi, with minimal gain variation across the frequency band. The study suggests implementing vertical beam steering for active antenna base stations. Most of the experiments mentioned involve multiple layers, and incorporating dual-polarization capability often requires sophisticated structures. In contrast, this study proposes achieving dual polarization using both +45° and -45° slanted radiating patch elements in a single layer, simplifying the design.

In [10], a dual-circularly polarized MIMO antenna was designed for a broad frequency range of 24.6 to 32.1 GHz, using just one layer. The highest gain achieved was 10.3 dBi, with an ECC (Envelope Correlation Coefficient) of 0.01 to minimize interference among ports. While the antenna provides a consistent radiation pattern when facing forward, its lack of adaptability may limit its usefulness in tasks requiring flexible or dynamic beam steering.

Research by [11] also created a dual-polarized antenna for millimeter-wave frequencies, intended for automotive radar and 5G communication. However, polarization switching relies on precise phase control across multiple ports, necessitating complex feeding networks or high-performance RF chips with phase-switching capabilities. This added complexity could increase costs, particularly for designs requiring basic circuitry.

Another study by [12] suggested a dual-polarized antenna operating in the frequency range of 29.5-30.5 GHz, relying heavily on accurate phase control to achieve the desired ±45° dual-polarized radiation. Manufacturing tolerances, material inconsistencies, or environmental conditions could disrupt polarization stability, reducing performance if phase alignment is not maintained, which could complicate implementation in real-world scenarios.

To achieve beam steering and wider spectrum coverage cost-effectively, this study aims to create a dual-polarized antenna using a single layer with potential gain at 28 GHz. The arrangement of antenna elements requires careful planning, as improper spacing between elements can lead to high mutual coupling, negatively impacting performance. Moreover, designing a dual-polarized antenna with beam steering requires careful consideration and the use of machine learning techniques to meet 5G specifications for lightweight, low-cost, low-profile, compact design, easy fabrication, and high isolation for mobile terminals [13].

Another study [14] investigates a compact 4 × 4 passive phased array antenna-in-package (AiP) with a low profile, consisting of patch antennas coupled with slots emitting left-handed circularly polarized (LHCP) radiation. Phase tuning is achieved using microelectromechanical systems (MEMS), allowing the primary beam to be directed across a range of ±30° in both vertical and horizontal planes between 28-30 GHz, with a gain of approximately 15 dB.

The primary goal of this study is to assess whether a neural network algorithm can effectively steer the main beam of the proposed dual-polarized antenna toward a desired direction. Various methods exist for redirecting the main lobe direction, with one popular approach involving the use of a Butler matrix, a beamforming network that directs signals to phased array antenna elements.

Research by [15] demonstrates a small 4 × 4 antenna system using a Butler matrix, printed on a two-layer Rogers Duroid substrate at the Ka-band, achieving beam-steering angles of ±4° and ±29° with gains of 14.5 dB and 13 dB, respectively. The demonstration shows the utilization of a field programmable gate array (FPGA) for a beam steering system, providing an alternative method for directing primary beams to a specific location. The system is abundant in resources, utilizes FPGA chips, and features multiple external connectors.

Mechanical and electronic phased arrays have been used to alter the radiation pattern of antennas, but they are generally considered unfavorable due to their weight, size, susceptibility to weather conditions, high costs, and mechanical failure due to fatigue and wear. In this study, phase control is the primary technique used to shape and scan the main beam radiation pattern for beam steering. Many studies have explored antenna arrays using various optimization techniques, such as hybrid methods and evolutionary algorithms [16]. However, as the number of antenna array elements increases, the computational time required to determine optimal weights grows. Thus, for time-sensitive tasks and large datasets, deep neural networks (DNNs) are an essential tool due to their computational efficiency.

DNNs are advanced neural networks with enhanced depth, complexity, and numerous layers and neurons, making them well-suited for large, complex systems. They can process multiple layers simultaneously, select features, and manage numerous parameters [17].

DNNs provide an effective computational method for expediting pattern synthesis while maintaining high accuracy, minimizing errors and processing time, and forecasting antenna performance. Researchers in [18] used a deep neural network to synthesize radiation patterns for a 4 × 1 patch antenna array, using the radiation pattern as input and the amplitude and phase of the antenna elements as output. The DNN generated radiation patterns that closely resembled the input, demonstrating the viability of deep learning for generating antenna radiation patterns.

In [19], a bone-shaped patch antenna (BSPA) for 5G applications at 28 GHz and 38 GHz was designed using a DNN model. The model was trained on 150 BSPA data points using a hybrid PSO and MGSA optimization technique, adjusting the learning rate to optimize the main beam shape and reduce sidelobe levels.

Research by [20] explored how deep neural machine learning can be used to develop radiation patterns for 8-element Active Electronically Scanned Array (AESA) antennas. The DNN model used 181 points of a specified radiation pattern as input and produced the phases of the array elements as outputs, significantly reducing dataset size and improving processing speed for real-time applications.

The study conducted by [21] suggests using the AEP method for a DNN database model, effectively directing the main beam in four different directions, though the approach has not been verified for larger array sizes. The Active Element Pattern (AEP) method offers several notable advantages, such as reduced complexity and computationally efficient. It enhances beam steering by accounting for mutual coupling effects, requires less data compared to full-wave modeling techniques, and is highly effective for large antenna arrays.

Previous studies in [22] explore the design of linear sparse arrays with varying sizes, including small-scale (4)-element) and large-scale (16-element) arrays, operating at a frequency of 5 GHz. The authors introduce the AEP technique for synthesizing both ideal arrays and arrays affected by mutual coupling. In [20], the AEP-DNN approach is applied to synthesize radiation patterns for 8-element antenna arrays at 10 GHz. Similarly, as investigated in [23], the feasibility of using DNNs for both direct and inverse modeling of 16-element antenna arrays at 3.5 GHz is examined. Additionally, the research in [24] includes a comparative analysis of three distinct DNN architectures using 8-element antenna arrays. In [25], the authors provide a comparative evaluation of various neural network (NN) architectures for implementing beamforming in 16-element antenna arrays. The demonstration of AEP and DNN across different array scales and frequencies highlights their scalability and adaptability for deep learning-based modeling.

This study proposes an AEP-driven method for generating training and validation radiation pattern data, which will serve as inputs for pattern synthesis using DNNs and compared to the other previous works shown in Table 4. The AEP-DNN approach employs a simple multilayer perceptron (MLP) and backpropagation network structure for model training. The primary focus of this research is beam-steering through the AEP-DNN approach, optimizing the phase of the array while keeping the amplitudes constant at 1. The study explores a

1 × 4 array antenna with ±45° dual linear polarization, four feed source ports, and 15.06 mm inter-element spacing, using dual-polarized radiating patch elements to evaluate beam-steering performance at 28 GHz.

The first section introduces the challenges at high frequencies, existing dual-polarized antenna designs, and the implementation of beam steering. Section II details the array antenna design using full-wave software and the fabricated array antenna. Section III describes the array antenna configuration, the AEP-based data collection method, the implementation of the AEP-DNN approach, and the experimental procedure for measuring beam steering using a built-in beamformer. Section IV discusses the results of beam-steering performance using the AEP-DNN method and the measured performance of the steered main beam. Finally, Section V summarizes the study's findings.

II. ARRAY ANTENNA DESIGN

To meet the 5G requirements, antenna design plays an important role. The size of the antenna depends on the operating frequency, substrate's dielectric constant, and height. The transmission feeding line and feeding method also need attention as they can affect the antenna performance. The material chosen is Rogers RT 5880 with a dielectric constant of 2.2 and a loss tangent of 0.0009. The substrate thickness used is 1.575 mm. The width and length of the radiating patch antenna, as well as the width and length of the substrate and ground plane, are calculated as follows [26]:

Calculation of the width of the patch:

$$W = \frac{\lambda_0}{2\sqrt{0.5(\varepsilon_r + 1)}} \tag{1}$$

Calculation of the effective dielectric constant:

For (W/h>1)

$$\varepsilon_{eff} = \frac{\varepsilon_r + 1}{2} + \frac{\varepsilon_r - 1}{2}\left(\frac{1}{\sqrt{1 + 12h/w}}\right) \tag{2}$$

where h is the thickness of the substrate.

Calculation of the length extension due to fringing:

$$\Delta L = 0.412 \times h\left(\frac{(\varepsilon_{eff} + 0.300)\left(\frac{W}{h} + 0.264\right)}{(\varepsilon_{eff} - 0.258)\left(\frac{W}{h} + 0.813\right)}\right) \tag{3}$$

Calculation of the length of the patch:

$$L = \frac{c_0}{2f_r\sqrt{\varepsilon_{eff}}} \tag{4}$$

$$L_{eff} = L - (2 \times \Delta L) \tag{5}$$

where L is the length of the patch before fringing correction and L_{eff} is the length of the patch after fringing correction.

Calculation of the width of the substrate and ground plane:

$$W_g = W + (6 \times h) \tag{6}$$

Calculation of the length of the substrate and ground plane:

$$L_g = L_{eff} + (6 \times h) \tag{7}$$

TABLE 1. The array antenna dimension.

Part	*The 1x4 ±45° dual linearly polarized (mm)*
Patch	2.4 x 4.2
Substrate	62.45 x 23.08
Ground	62.45 x 23.08

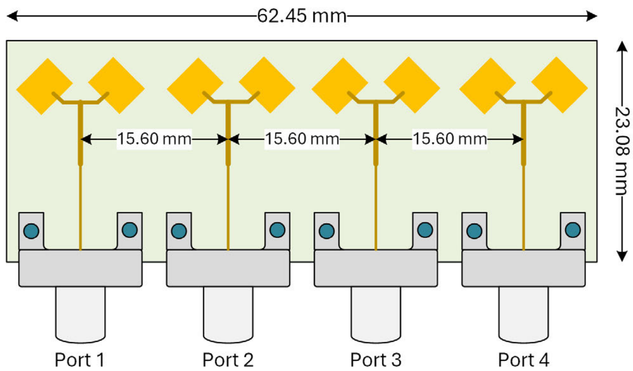

FIGURE 2. The illustration of 1 × 4 ±45° dual linearly polarized array antenna.

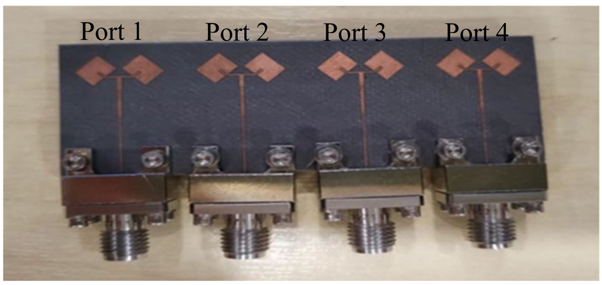

FIGURE 3. The fabricated array antenna.

In this work, the inset feeding method and edge coaxial feeding are chosen. The possible factor in choosing a feeding method is the efficient transfer of power between the radiating structure and the feeding structure [27]. The characteristic impedance, the input resistance, the conductance of the patch in its transmission line model, and the notch width are calculated based on [28]. The element spacing for a 1 × 4 array antenna is greater than 0.5 λ (2.159λ); which is approximately 15.60 mm. The 2.92 mm SMA connector is relatively large, requiring us to arrange the antenna element to accommodate its size. Table 1 shows the dimensions of the array antenna. Fig. 2 shows the illustration of a 1 × 4 ±45° dual linearly polarized array antenna (DLPAA) design using full-wave modelling software (CST). Fig. 3 shows the fabricated array antenna.

Before applying the proposed AEP-DNN method, the S-parameters of the array antenna have been simulated and measured. Fig. 4 and 5 show the results of the reflection coefficient and mutual coupling of the array antenna.

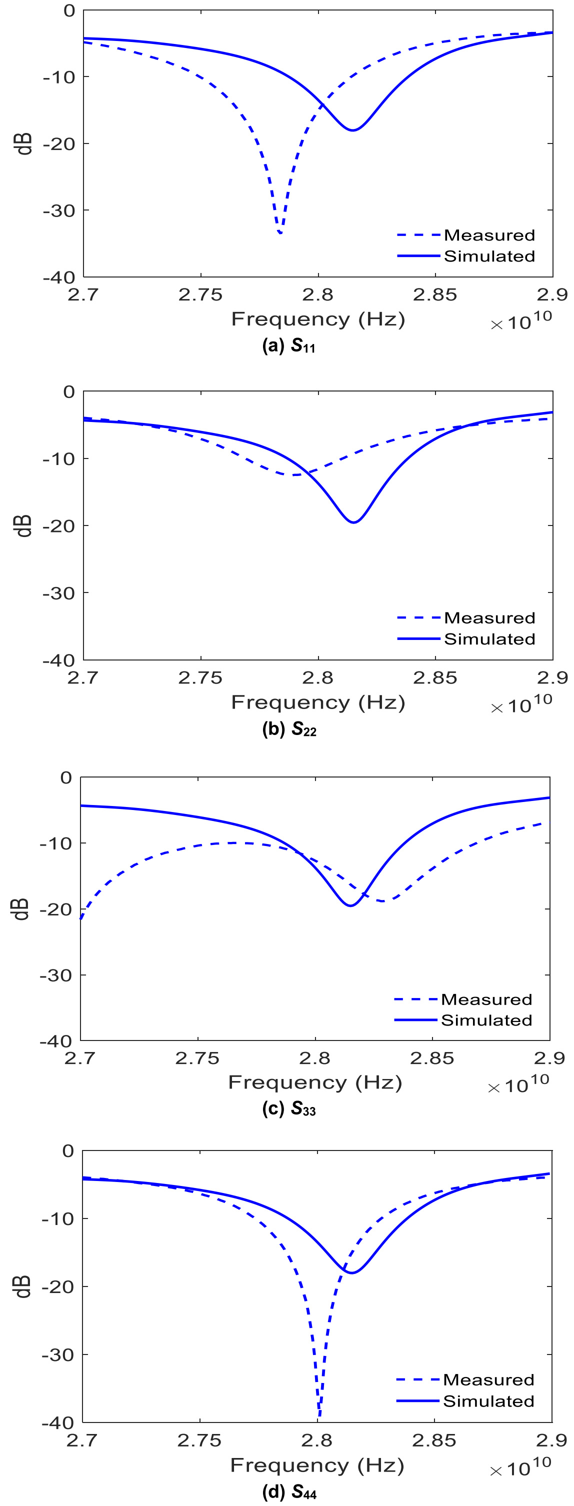

(a) S_{11}

(b) S_{22}

(c) S_{33}

(d) S_{44}

FIGURE 4. The reflection coefficients of the array antenna for each port.

As shown in Fig. 4, the simulated reflection coefficient at 28 GHz for port 1, port 2, port 3, and port 4 is −13.44 dB, −13.66 dB, −13.67 dB, and −13.43 dB. The measured reflection coefficients at 28 GHz for port 1, port 2, port 3, and port 4 are −15.05 dB, −11.57 dB, −12.69 dB, and

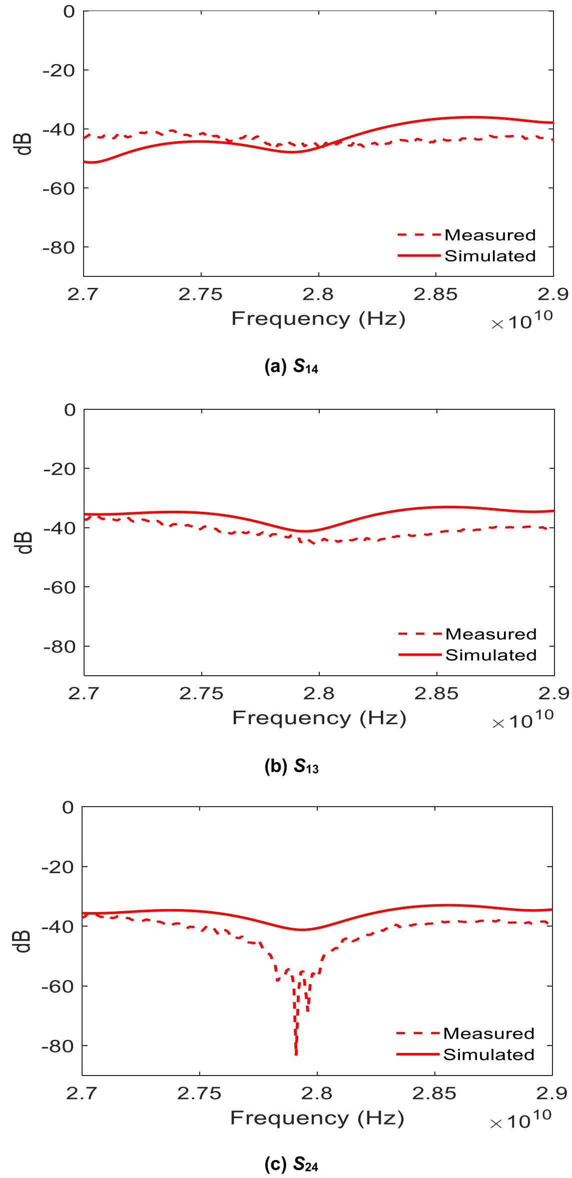

(a) S_{14}

(b) S_{13}

(c) S_{24}

FIGURE 5. The mutual coupling of the array antenna.

−35.23 dB respectively. Both the simulated and measured reflection coefficients show good performance; however, the frequency is shifted slightly upwards at 28.15 GHz for the simulated reflection coefficient and downwards and upwards within the range of 27.00 GHz to 28.01 GHz for the measured reflection coefficient. A slight difference between the shifted frequencies and the desired resonant frequency of 28 GHz might be due to fabrication errors.

III. DEEP NEURAL NETWORK

Machine learning and deep learning have many similarities, but the main difference is that deep learning integrates feature gathering and regression/classification, involves a higher quantity of neurons, operates on data simultaneously through various layers, extracts feature essentially, and assesses

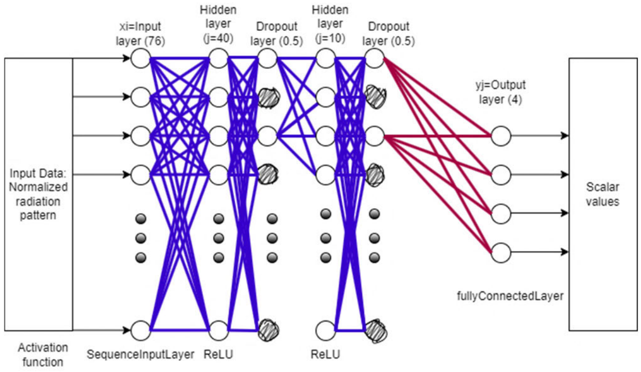

FIGURE 6. **The proposed 6-layer DNN framework.**

optimal network hyperparameters. The information is transmitted to the neurons in the multi-layered hierarchy, which then pass this processed data to subsequent layers to construct a more useful learning framework.

Multilayer perceptions, also known as MLPs, consist of multiple hidden layers within a deep neural network structure. MLPs have been utilized in diverse applications and incorporated in this study. Several algorithms like Levenberg-Marquardt (LM), back-propagation, and others are utilized for training the learning model. Adaptive Moment Estimation (ADAM) optimizer is utilized for model training in this research. ADAM is the latest algorithm that is computationally efficient and faster, as it computes learning rates for each parameter. This algorithm is particularly valuable when dealing with optimization problems that involve large volumes of data or high numbers of parameters [29]. Fig. 6 illustrates a DNN framework architecture of an MLP model that has 6 layers; an input layer, two hidden layers, two dropout layers, and an output layer.

The neurons in the hidden layer only act as buffers for distributing input signals x_i, not performing any actual computations. In every hidden layer neuron j, the input signals x_i are added together with their corresponding input layer connections w_{ji}, and the outputs y_j are calculated based on this sum [30];

$$y_j = \mathrm{f}\left(\sum w_{ji} \times x_i\right) \tag{8}$$

In this study, the linear activation function of a ReLU layer is used instead of a simple threshold function $f(\cdot)$. Neural output is generated from every layer. ADAM is a common tool utilized for adjusting the weights of MLP networks during the training process. The ADAM learning process outputs the change in weight between neurons i and j in a network. The weights are modified using the formula suggested by [19].

The number of epochs in the training network is 2000. Furthermore, the input layer, hidden layer, and output layer all used the *SequenceInputLayer*, *ReLU,* and *fullyConnectedLayer* functions respectively. The neurons containing information are then placed into the input layer and all of these neurons operate independently. The Multilayer Perceptron (MLP) network used in the learning process is a feed-forward neural network where each hidden node's activation is controlled. This repetitive procedure utilizes the back-propagation technique.

A. ARRAY ANTENNA CONFIGURATION

Fig. 2 illustrates the antenna design structure for the radiation pattern simulation corresponding to the input signal of each antenna element. The 1 × 4 ±45° dual linearly polarized array antenna was designed using full wave software. The substrate material used was Rogers RT5880 with a relative permittivity of 2.2 and a thickness of 1.575 mm. The patch antenna has a length and width of 2.4 mm and 4.2 mm, respectively. The edge feeding method used is a transmission line model using an SMA connector of 50 Ω for each port. The operating frequency of the antenna is 28 GHz. The mutual coupling between antenna elements was chosen with the distance inter-elements being equal to 15.60 mm.

B. TOTAL ELECTRIC FIELD USING AEP METHOD

Importantly, the beam-steering capability depends on the direction of the main beam signals. These main beam signals are directed to the desired location by controlling the antenna phase value [31]. AEP calculation was used to calculate the training and validation data for the DNN inputs. The total electric field is the AEP of the array antenna for each number of ports (AEP_n) as shown in Eqs. 9 and 10 [32]. In this study, the amplitude (I_n) was fixed to 1, and phases ($\emptyset_n$) were varied for each port [33].

$$E_{total} = \sum\nolimits_{n=1}^{4} I_n \times AEP^n \times (\theta, \varphi) e^{jk \times a_n \times cos(\emptyset_n) \times sin\theta} \tag{9}$$

$$a_n = \left(n - \frac{N+1}{2}\right) d, \quad n = 1, 2, 3, 4. \tag{10}$$

I_n is the complex value of feed current applied to the nth element, $AEP^n(\theta, \varphi)$ is the electric field value at each nth port within the θ range $-175°$ to $180°$ at cut angle phi, φ of 90° which is obtained from the full wave model. k is the constant wavenumber, $k = 2\pi f \sqrt{DE} \Big/ c$, ($c = 3x10^8 m/s$, $f = 28GHz$, DE = 2.2); d is the inter-element spacing, $d = 15.60mm$, $\emptyset$ is the phase; θ is the theta range $-175°$ to $180°$ with a step size of 5°. The average time taken to generate one sample of radiation pattern using the AEP method is approximately 1 sec/frame.

The ASCII files of the electric field were exported in post-processing columns for each port (port 1 to port 4). These ASCII files contain real absolute numbers in 5° theta intervals. The extracted ASCII file for port 1 is the absolute E-field at port 1, called AEP1. Similar steps were taken for other ports resulting in AEP2, AEP3, and AEP4. The total number of absolute E-field values at each port is 72, covering 72 theta angles from $-175°$ to $180°$.

All extracted AEP values for each port were then imported into an Excel file named "AEP.xlsx". This Excel file was intended to serve as input variables for MATLAB

TABLE 2. The amplitude and phase input signals for the training data set.

Port	*Amplitude*	*Phase*	*Number of cases*
1	1	0°	1
2	1	0°,20°,40°,…,340°,360°	19
3	1	0°,20°,40°,…,340°,360°	19
4	1	0°,20°,40°,…,340°,360°	19

TABLE 3. The amplitude and phase input signals for the validation data set.

Port	*Amplitude*	*Phase*	*Number of cases*
1	1	0°	1
2	1	10°,50°,90°,130°	4
3	1	10°,50°,90°,130°	4
4	1	10°,50°,90°,130°	4

programming to analyze the radiation pattern of training and validation data using Eqs. 9 and 10. The training, validation, and test datasets were carefully kept separate to ensure data reliability, accuracy, and unbiased results.

The phase of Port 1 was set to 0°, and the phases of the other ports were compared with it. By incrementing the phase input signals by 20°, the training data was processed. This resulted in 19 cases being generated for the training data, so the total number of radiation patterns is 1 × 19 × 19 x 19 = 6,859. The validation data and training data were kept distinct to validate the network.

Data collection for the initial phase of validation began at 10°, increased by 40°, and ended at 130°. This produced 4 cases, so the total number of radiation patterns is 1 × 4 × 4 × 4 = 64. Tables 2 and 3 illustrate the amplitude and phase input signals of the array antenna for each training and validation dataset.

For the test phase dataset, the amplitude (I_n) was set to 1 and the port's phase was determined by the phase shift difference between adjacent ports. The desired main beam direction, θ, was set at 5°, and 10° and inputted into Eq. 11 to obtain the phase value, β. The desired pattern is an ideal square-shaped radiation pattern that could not be generated from the array antenna but was used as the desired input pattern.

$$\beta = k \times d \times cos(\theta) \tag{11}$$

The collection of radiation pattern data by AEP computation, which consists of the collected training and validation data, was in complex integer values and serves as the input to the DNN model. These inputs would go through preprocessing data to be converted into a scalar value ranging from 0 to 1 with a total of 72 input data. The preprocessing data was carried out by taking the absolute value of collected training and validation data, then dividing by its maximum value of data at each $\theta°$ interval ($-175°$:5°:180°) to normalize the input variables ranging from 0 to 1.

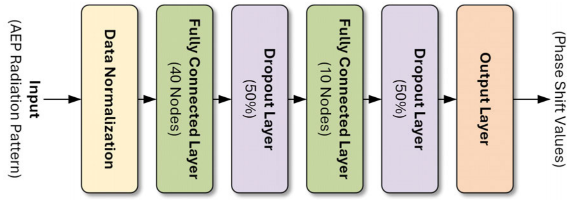

Algorithm 1 Training AEP-DNN Model for Beam-Steering

```
Initialize: Clear MATLAB workspace
Load dataset: AEP.xlsx
Extract input data X (radiation patterns) and output labels Y (phase values
  for 4 antenna elements)
Normalize X: X ← (X−min(X))/(max(X)−min(X))
Define Neural Network Layers:
  Input Layer: sequenceInputLayer(inputSize)
  Hidden Layer 1: fullyConnectedLayer(40)
  Activation: ReLU
  Dropout Layer (50% neurons removed)
  Hidden Layer 2: fullyConnectedLayer(10)
  Activation: ReLU
  Dropout Layer (50% neurons removed)
  Output Layer (fullyConnectedLayer(1))
Set Training Parameters:
  Optimizer: Adam
  Maximum Epochs: 2000
  Mini-batch Size: 10
  Learning Rate: 0.001
  Validation Data: (X,Y)
  Training Progress Plot: Enabled
Train the Network:
Train the model using trainNetwork(X, Y, layers, "mse", options)
Save trained model as AEP_DNN_Model.mat
Output: Display training completion message
Predict the Model:
Predict the Model using minibatchpredict(net,X)
```

FIGURE 7. AEP-DNN algorithm for beam-steering.

C. FEEDFORWARD-MLP AEP-DNN-BASED METHOD OF MODELLING, TRAINING, VALIDATING, AND TESTING NETWORK

Fig. 6 displays the architecture of the DNN framework, which includes the input and output of the DNN. The type of input and output is essential as the learning algorithm depends on these types of inputs and outputs. The radiation pattern of training and validation data obtained from the AEP method was in units of 5° ranging from -179° to 180°. These data were inputted into the DNN model. The DNN output data of predicted phases were expressed in radians.

The DNN framework consists of 6 layers. The input, hidden, and output layers are ''sequenceInputLayer'', ''ReLU'', and ''fullyConnectedLayer''. The ''dropoutLayer(0.5)'' was also used to avoid overfitting learning data, with 0.5 being set by default. Each layer employs a dense layer that connects input and output neurons completely. The number of neurons in each hidden layer was 40 and 10, respectively. To analyze the performance of the AEP-DNN-based method, root-mean-squared-error (RMSE) and loss performance were obtained. The ADAM optimizer was used. The number of epochs was set to 2000. The batch size was set to 50. Fig. 7 shows the AEP-DNN algorithm for the whole process.

To observe the effect of the number of neurons and epochs on the DNN model performance including training and validation RMSE and loss plots, a few sets of selection samples of neurons and epochs have been investigated and discussed in Section IV (part C). The selection sample of the number of neurons in the first and second hidden layers are 50 and 10, and 100 and 10, respectively, and the number of epochs is 2500, and 3000.

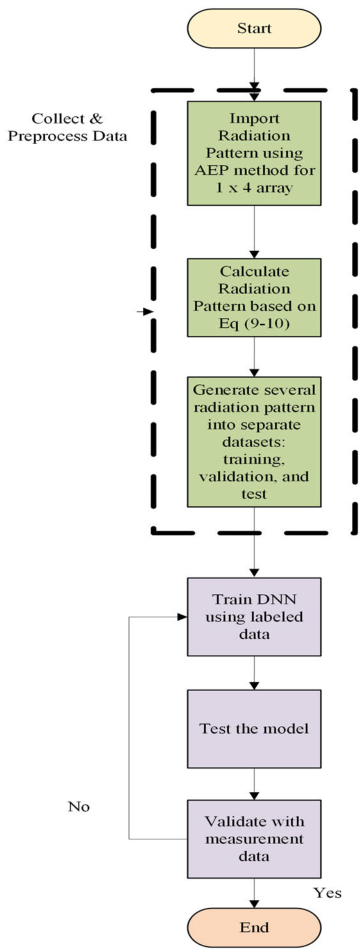

FIGURE 8. Flowchart for AEP-DNN method.

MATLAB version 2024a was used for the computation of the AEP-DNN-based method. It took approximately 2 to 3 minutes to train the AEP-DNN model when using the hardware specification of the AMD Ryzen 3 3200U with Radeon Vega Mobile Gfx 2.60 GHz and a memory of 8GB.

The DNN model was developed through a computational approach using a few sets of hyperparameters, and the input variables were assigned to the DNN model. The input training dataset was assigned as the "XTrain" and "YTrain" variables, the input validation dataset was assigned as the "XValidate" and "YValidate" variables, and the input test dataset was assigned as the "XTest" and "YTest" variables. The "X" variable indicates the input radiation pattern, while the "Y" variable indicates the input phases.

In general, the whole AEP-DNN process has been summarized in the flowchart of Fig. 8. It is applicable for any size of arrays. However, different size of antenna array requires a slight modification at the initial stage as the AEP patterns need to be imported from full wave software into Matlab. Then, the dataset can be generated using eq. 9. Nevertheless, the AEP pattern becomes increasingly accurate with an increasing number of arrays [33].

D. CALIBRATION PROCEDURES

Before conducting any experiments, a calibration procedure must be carried out to ensure accurate beamforming. For the antenna array, a standard calibration process has been performed using open, short, load, and through (SOLT) calibration with a Keysight VNA to measure S-parameters. This measurement has been conducted separately in the anechoic chamber, UTM Semarak.

On the other hand, the pattern measurement was calibrated first using a standard antenna array, and the measured radiation pattern was validated using a lookup table provided by the manufacturer. Then, the standard antenna array has been replaced with an antenna under test (AUT). The measurement procedure was conducted at the RF Station due to the availability of the beamformer and anechoic chamber.

E. S-PARAMETERS AND PATTERN MEASUREMENT

To verify the proposed AEP-based method, a beamformer is used to excite and tune the input phases of the Dual-linearly polarized array antenna (DLPAA). TMYTEK 5G FR2 beamformer with 1×4 RF ports [34] is used for array antenna verification. It is equipped with a software-controllable phase shifter which offers 5.625 deg resolution and makes the board a versatile beamformer. Four independent RF channels synthesize beams by adjusting the phase and amplitude of each channel. The intuitive GUI TMXLAB Kit (TLK software) connects the beamformer via the LAN port to control the phase and amplitude of each RF port to form the beams. Fig. 9 shows the top view of the built-in beamformer, the connection of DLPAA with the built-in beamformer, and the chamber.

The R2 Compact Antenna Test Range (CATR) chamber is a light type provided by Atenlab [35] which operates from 10-80 GHz. The interior is lined with RF absorbers to minimize reflections during testing. A Device Under Test (DUT) positioner allows for movements in 0.1° increments, facilitating precise measurements. It is equipped with Atenlab's Maxwell and Maxwell Lite software that automates the measurement process and can present collected data in 2D and 3D formats.

IV. RESULTS AND DISCUSSION

This section discusses the results obtained using the AEP-DNN method. This includes verification of AEP with PMM and full-wave methods, AEP-DNN algorithms, sensitivity analysis, computational complexity, environmental factors, and verification with measurement method.

A. VERIFICATION OF AEP WITH PMM AND FULL WAVE METHODS

It is crucial to verify the reliability of the AEP method by the Pattern Multiplication Method (PMM) using MATLAB and the full-wave model. Therefore, one sample dataset was chosen. The amplitude (I_n) was fixed at 1. The phase of the array antenna in the validation data was selected as follows: antenna port 1: 10°, antenna port 2: 50°, antenna port 3: 90°, and antenna port 4: 10°.

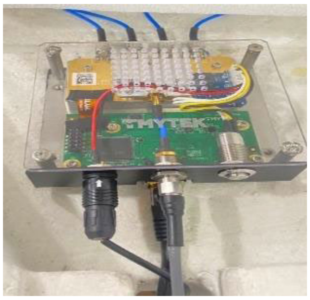

(a) The top view of beamformer

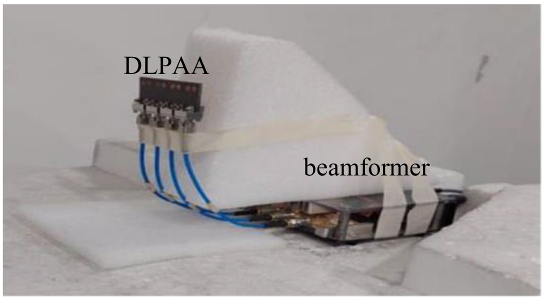

(b) The connection of DLPAA with the built-in beamformer

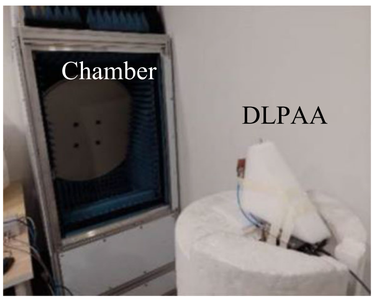

(c) The chamber

FIGURE 9. The beam former and array antenna setup for measurement.

The radiation pattern for the given data was derived using the AEP method before implementing DNN. The AEP (with coupling) was obtained from the 3D Simulation tool and calculated based on Eq (9)-(10) using identical amplitude and phase values. The array radiation pattern (no coupling) was computed based on the pattern multiplication method (PMM) using fixed amplitude and varied phase values, calculating the array factor for each phase input [36] and then multiplying it with the single element pattern.

Fig. 10 displays the PMM, AEP, and numerical patterns for the phase dataset that was chosen. The peak gain and radiation pattern shape for the above methods are in good agreement with each other. Hence, this AEP technique has been confirmed as effective and subsequently integrated into the AEP-DNN approach. The verification of the method is also plotted in a finer step size of 1° of theta angle.

B. AEP-DNN FOR BEAM-STEERING METHOD

Two test datasets with the target main beam angles of 5° and 10° were chosen for testing the network. An ideal

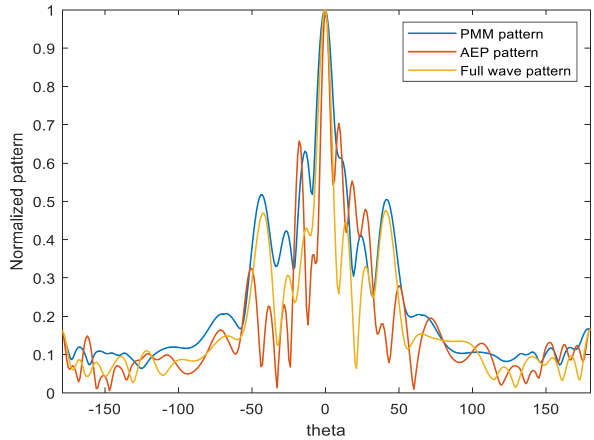

FIGURE 10. Verification of the AEP with PMM and numerical method sat phases of 10° 50° 90° 10°.

square-shaped input pattern with a gain of 1 was fed into the DNN model, having a 10° beamwidth and -5 dB side lobe level. The data pattern AEP-DNN was generated by including the predicted phases in the AEP calculation using MATLAB. The AEP-DNN, PMM, and numerical designs were generated by utilizing the estimated phase DNN results as their input phases. Fig. 10 displays the radiation pattern based on the desired, the predicted AEP-DNN, the PMM, and the numerical methods in normalized forms where the maximum value of 1 represents the main beam location.

Fig. 11 shows that the main beams of predicted AEP-DNN, PMM, and full wave patterns are matched and fall within the main beam of the desired pattern. The plotted graphs are also in a finer step size of 1° theta angle.

The elapsed processing time for learning the DNN algorithm is approximately 2 to 3 minutes. Based on Fig. 12, the training and validation RMSE and loss converge to a minimum value of 1.3 to 2.3. The closer the minimum RMSE and loss values are to '0', the better the convergence rate of both training and validation performances. The selection sample of the number of neurons in the first and second hidden layers are 50 and 10, and 100 and 10, respectively, and the number of epochs is 2500 and 3000.

The AEP-DNN method accurately predicts the required main lobe direction phases, outperforming array factor theory in terms of accuracy and good agreement with the numerical study. The rise in accuracy suggests that the neural network considers the impact of coupling when predicting phases.

C. SENSITIVITY ANALYSIS

To evaluate the impact of the number of neurons and epochs on the performance of the DNN model, including training and validation RMSE as well as loss plots, various selected neuron and epoch configurations were analyzed, as shown in Fig. 13.

Additionally, the influence of neurons and epochs on the model's convergence performance was examined to justify

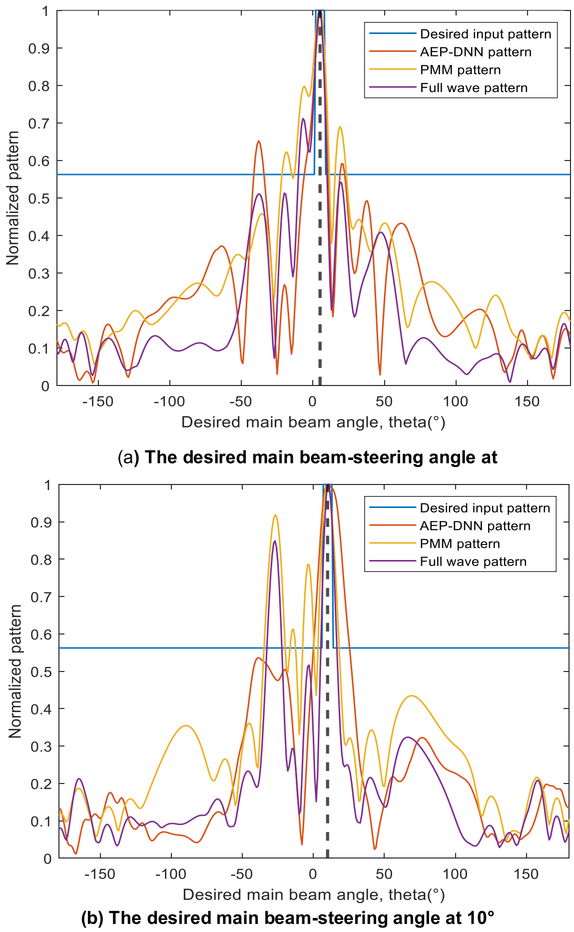

FIGURE 11. The comparison between desired, AEP-DNN,PMM, and numerical radiation patterns.

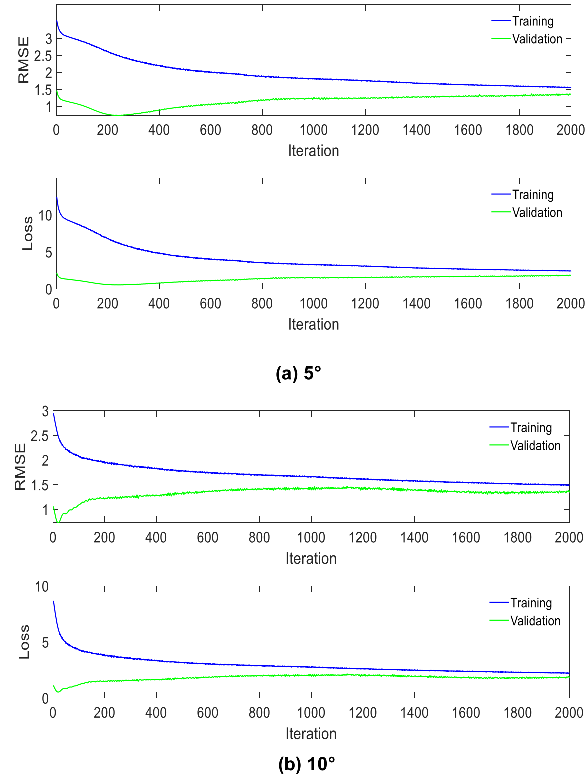

FIGURE 12. The training and validation RMSE and loss.

the selection of 40 and 10 neurons and 2000 epochs for this study, as illustrated in Figs. 13 and 14. It shows that the varying number of neurons lowers the convergence of both RMSE and loss training plots from the original set of neurons of 40 and 10 meanwhile the convergence of both RMSE and loss validation plots are not affected. However, there is a minimal difference in convergence performance between those sample sets and the chosen set of neurons except that the processing time to execute the outputs is much longer with an increasing number of neurons. The varying number of epochs is also set to 2500 and 3000 based on Fig. 12. It is essential to carefully monitor training and validation RMSE and loss plots when increasing the number of epochs, as this may lead to underfitting or overfitting. The figure indicates that increasing epochs from 2000 to 2500 moves closer to the intercept point at the final iteration. However, when the number of epochs reaches 3000, the model exhibits overfitting, as evidenced by validation plots exceeding training plots at the end of the iteration. Given the specific hyperparameters and dataset, using 3000 epochs poses a significant risk.

The optimal number of epochs should be determined based on the initial training and validation data, along with other hyperparameters. A higher number of epochs may be more suitable for larger datasets. It is essential to carefully select the appropriate sets of neurons and epochs, as previously outlined in this study.

D. COMPUTATIONAL COMPLEXITY

The AEP-DNN training process requires approximately 2-3 minutes, while inference time per sample is less than 10 milliseconds, making it feasible for real-time beam-steering applications. The memory footprint of the trained model is ∼5MB, 4.89% of CPU utilization indicates low power consumption using the command prompt tool providing energy report analysis, and the CPU priority level is 8 reported by Sysinternals Process Explorer which indicates the normal level. CPU Priority and Power Consumption are related because higher-priority processes demand more CPU time, which can lead to increased power usage.

E. ENVIRONMENTAL FACTORS ON PHASE PREDICTIONS

Nevertheless, there is no way to fully avoid other potential noise and environmental factors, such as receiver thermal noise that decreases the signal-to-noise ratio (SNR), resulting in inaccurate phase estimations [37]. Inaccurate phase estimations could also be caused by environmental factors such as multipath effects, atmospheric conditions, and electromagnetic interference [38], [39], [40]. For this reason, every possible precaution is taken when measuring to ensure that all the factors that may adversely affect the reliability of the

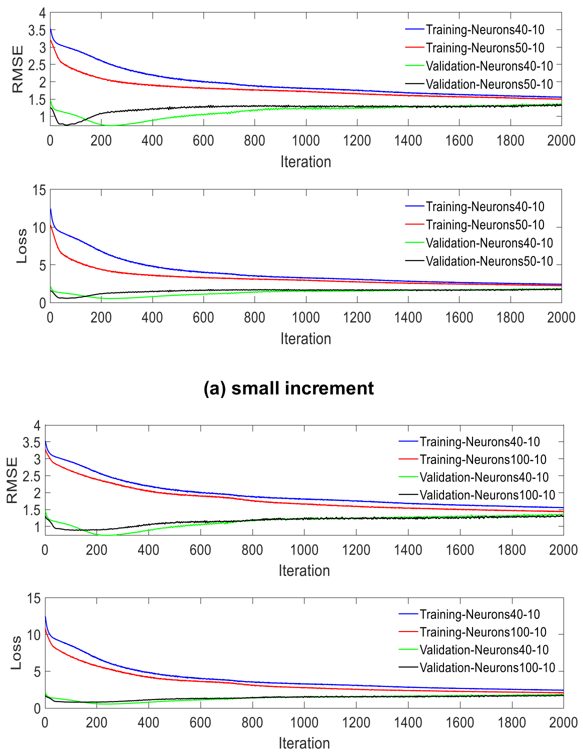

(a) small increment

(b) large increment

FIGURE 13. **The RMSE and loss convergence plots on different number of neurons.**

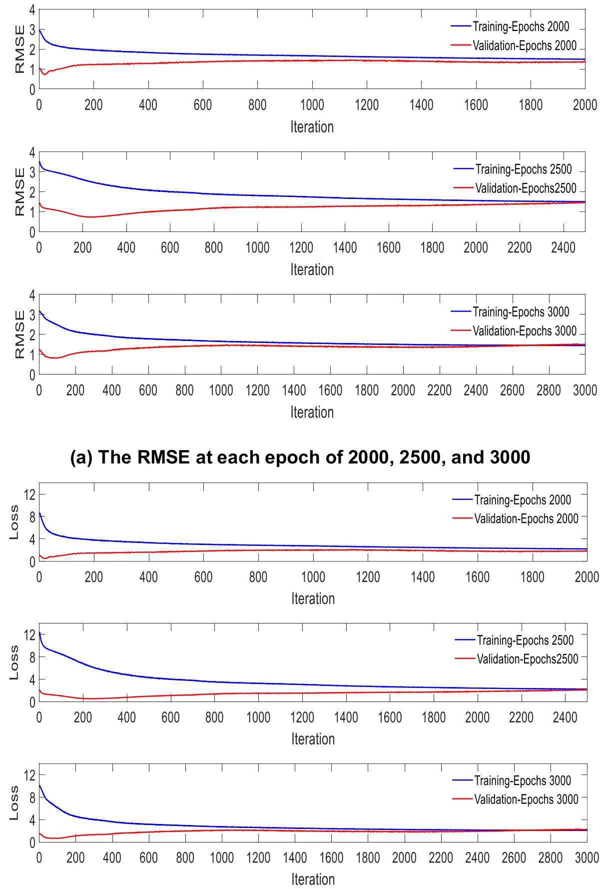

(a) The RMSE at each epoch of 2000, 2500, and 3000

(b) The loss at each epoch of 2000, 2500, and 3000

FIGURE 14. **The RMSE and loss convergence plots on different number of epochs.**

phase prediction are minimized. Measurement is conducted without anyone using the experimental setup firsthand to reduce the prolonged temperature coming from the receiver. A nearby object like metal or electronic devices that can interfere with the signals is also taken into consideration.

This suggested that the AEP-DNN method is effective. The DNN displays excellent learning, generalization, parallel processing, and error endurance capabilities, making it the perfect choice for modeling nonlinear mappings of intricate data in various applications.

F. VERIFICATION OF AEP WITH MEASUREMENT

This approach utilizes an AEP-DNN that can be taught to deal with various quantities of elements, spacing, and excitation. The beamformer's input phases are tuned to steer the main beam into a desired location. The input phases for each desired angle at 0°, 11°, and 25° for ports 1-4 are {0°,0°,0°,0°}, {130°,85°,45°,0°}, and {250°,170°,85°,0°} respectively. The measured pattern after tuning the phases is compared to the numerical and AEP patterns as shown in Fig. 15.

Based on Fig. 15, the array antenna has been successfully steered into the desired main beam angle given the input phases using the beamformer. The measured radiation pattern of the desired angle matched with the numerical and AEP patterns, even though the sidelobes are different from each other. It might be caused by the placement of the array antenna on the antenna holder, the interference losses, and the experimental surroundings of the half-wave chamber. The discrepancies between sidelobes of measured, numerical, and AEP pattern might be also influenced by the computation of AEP is more accurate for the large arrays. However, this method focuses on the implementation of a neural network for beam-steering purposes. In future work, the AEP computation can be upgraded to include the ground edge effects [41].

In addition to the abovementioned factors, several other reasons could be the potential sources that lead to measurement discrepancies such as due to the chamber conditions such as some residual reflections that can cause unwanted interference, affecting sidelobe levels. Other than that, misalignment of the antennas (feed and array antennas-DUT) that are not centered properly can affect sidelobe levels and pattern distortion. Variations in RF cable bending, loss, or movement can also lead to amplitude and phase variations, affecting sidelobe consistency.

Moreover, the AEP method becomes increasingly accurate as the number of elements in the array increases. However, since the beamformer provided by TMYTEK has 4 output ports, we only developed the system for a 1×4 antenna array.

TABLE 4. Comparison of this work and previous works.

Papers	*Aim*	*Methods*	*DL Structure*	*Data for the DNN model*	*Steered-main beam*	*Train/Validation loss*
[18]	Pattern synthesis in response to an ideal input radiation pattern	-simulations using ANSYS/HFSS -TensorFlow 2.0 for DL	-4 elements -linear polarization -liner, ReLU activation functions -ADAM -epochs 500 -5 layers	-6859 (training) -64 (validation) -step size 1° -theta angle = (0°-180°) -E-plane -input value = 181	114°	0.00022/0.00026
[19]	Pattern synthesis in different directions with high gain and low sidelobe levels of -30 dB	-simulations using CST for DNN database and linked to MGSA-PSO algorithm, MATLAB coded for initial phases to feed DNN model	-16 elements -circular polarization -tangent sigmoid, sigmoid, purlin activation functions -epochs 150 -5 layers	-135 (training) -15 (validation) -step size 15° -theta angle = (0°-360°) -input = 24-bit binary code	40°, 142°, 205°, 320°	Not reported
[20]	Pattern synthesis	-simulation using CST -validation using MATLAB and CST -phase obtained from the progressive phase shift equation	-8 elements -linear polarization -ReLU activation functions -ADAM -epochs 500 -10 layers	-6859 (training) -64 (validation) -step size 1 -theta angle = (0°-180°) -E plane -input = 181	120°, 70°	0.0006/0.0008
[21]	Pattern synthesis using AEP	-CST simulation for input phases	-12 elements -linear polarization -ReLU and batchnorm activation functions -ADAM -epochs 150 -14 layers	-8640 (training) -2160 (validation) -step size 1° -theta angle = (-30°-30°) -input = 2	25°, 15°	Not reported
This work	**Pattern synthesis using an AEP-based method for the DNN database**	**-validation using full wave modelling (CST), and pattern multiplication method** **-train the DNN model using MATLAB**	**-4 elements** **-linear polarization** **-ReLU, dropout, and linear activation functions** **-ADAM** **-epochs 2500 & 2000** **-6 layers**	**-6859 (training)** **-64 (validation)** **-step size 5°** **-theta angle = (0°-360°)** **-input = 72**	**5°, 10°**	**2.26/1.77** **1.50/1.33**

Table 4 elaborates on the comparison of this work with the previous work.

The significance of this work states the need for a more accurate optimization technique over conventional methods. Conventional optimization methods like full-wave modelling require a large processing time and are impractical for handling large amounts of data. On the other hand, an array analysis using the pattern multiplication method (PMM) is simpler yet does not include mutual coupling which might be inaccurate for small dimensions of arrays. This could lead to significant errors in antenna pattern synthesis, especially at higher frequency bands of 5G. The AEP-DNN method can steer the beam in the desired direction with training and validation loss between 1.3 to 2.2, which is considered a low convergence rate.

V. CONCLUSION

The AEP-DNN approach was created to generate the radiation pattern for a 28 GHz ±45° dual linearly polarized array antenna with 4 radiating patch elements. A deep neural network was built with the radiation pattern as input and the antenna phases as output. The suggested approach, which was trained and validated with 6859 and 64 pattern data respectively, demonstrates strong performance in creating the

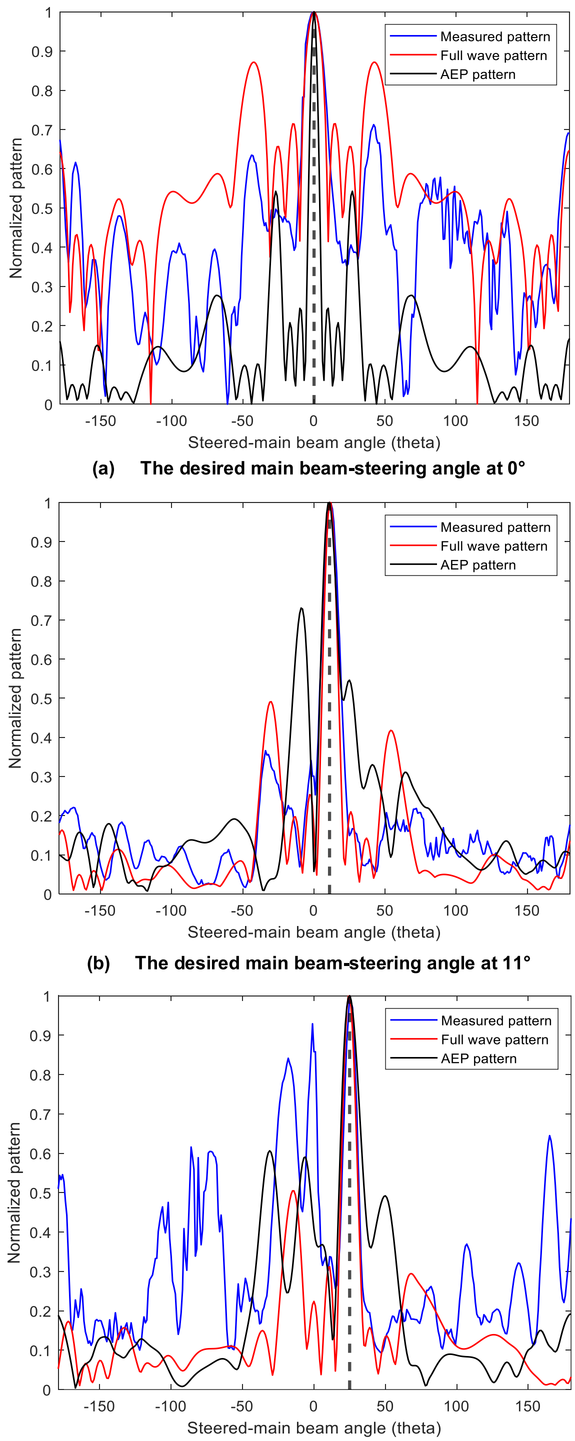

(a) The desired main beam-steering angle at 0°

(b) The desired main beam-steering angle at 11°

(c) The desired main beam-steering angle at 25°

FIGURE 15. The comparison between measured, PMM, and numerical radiation patterns.

desired patterns. The findings confirmed that the radiation pattern obtained from the pattern multiplication and numerical/full wave method closely matched the input radiation pattern calculated by AEP. The test results of the AEP-DNN method with low complexity show that it is suitable for the ideal square radiation pattern. To summarize, the AEP-DNN model was used to steer the main beam of the array antenna towards a specific angle. The findings indicate that the desired patterns align with the synthesized ones. This showed that deep learning is a dependable method for radiation pattern synthesis. The antenna pattern synthesis has been conducted using a combination of the DNN model and AEP-based method which considers of mutual coupling effect. Instead of using the same approach of applying the full wave model to get the initial approximation of input phases to the DNN model, this study suggests an alternative method using the AEP approach for better reliability and feasibility in pattern synthesis performance. The main benefit of the DNN-based method compared to the traditional analytical method is faster computation time, as the dataset has already been trained. When combined with the AEP method, it not only enhances efficiency but also maintains the same level of accuracy as full wave modelling and other analytical techniques, as it includes a mutual coupling effect between antenna elements. In addition, the measurement of the array antenna to observe its beam-steering capability using the beamformer to validate the AEP method has been successfully achieved. In future research, the potential of the AEP-DNN method could be further explored for MIMO antenna usage.

ACKNOWLEDGMENT

The authors would like to express their gratitude to the Ministry of Higher Education, International Islamic University Malaysia (IIUM), and RF Station for providing the facility to do measurement and their support. They are also acknowledging the use of AI from "ChatGPT" for grammatical enhancement in the abstract and introduction sections.

REFERENCES

[1] A. F. Kaeib, N. M. Shebani, and A. R. Zarek, "Design and analysis of a slotted microstrip antenna for 5G communication networks at 28 GHz," in *Proc. 19th Int. Conf. Sci. Techn. Autom. Control Comput. Eng. (STA)*, Mar. 2019, pp. 648–653.

[2] M. Y. Mohamed, A. M. Dini, M. M. Soliman, and A. Z. Md. Imran, "Design of 2 × 2 microstrip patch antenna array at 28 GHz for millimeter wave communication," in *Proc. IEEE Int. Conf. Informat., IoT, Enabling Technol. (ICIoT)*, Feb. 2020, pp. 445–450.

[3] M. U. Tahir, U. Rafique, M. M. Ahmed, P. Dalal, S. Agarwal, and S. M. Abbas, "Semi-ring patch array antenna for high gain 28 GHz applications," in *Proc. IEEE Wireless Antenna Microw. Symp. (WAMS)*, Jun. 2023, pp. 1–3.

[4] R. Yadav, A. Parmar, L. Malviya, and D. Nitnaware, "28 GHz inset feed circular shaped compact patch antenna array for 5G wireless communication," in *Proc. 10th IEEE Int. Conf. Commun. Syst. Netw. Technol. (CSNT)*, Jun. 2021, pp. 1–4.

[5] K. A. Alblaihed, Q. H. Abbasi, M. A. Imran, and L. Mohjazi, "Wideband of microstrip patch antenna for 28 GHz 5G applications," in *Proc. IEEE Int. Symp. Antennas Propag. USNC-URSI Radio Sci. Meeting (USNC-URSI)*, Jul. 2023, pp. 189–190.

[6] A. A. Almohammedi, A. Raad, S. Darshi, V. Shepelev, M. H. M. Yusof, and M. Balfaqih, "High gain and efficiency triple U-shaped slots microstrip patch antenna for 5G applications," in *Proc. 3rd Int. Conf. Comput. Inf. Technol. (ICCIT)*, Sep. 2023, pp. 573–576.

[7] K. Cuneray, N. Akcam, T. Okan, and G. O. Arican, "28/38 GHz dual-band MIMO antenna with wideband and high gain properties for 5G applications," *AEU-Int. J. Electron. Commun.*, vol. 162, Apr. 2023, Art. no. 154553, doi: 10.1016/j.aeue.2023.154553.

[8] A. Qayyum, A. H. Khan, S. Uddin, O. Ahmad, J. S. Khan, and S. Bashir, "A novel mmWave defected ground structure based microstrip antenna for 5G cellular applications," in *Proc. 1st Int. Conf. Smart Syst. Emerg. Technol. (SMARTTECH)*, Nov. 2020, pp. 28–31.

[9] K. A. Fante and M. T. Gemeda, "Broadband microstrip patch antenna at 28 GHz for 5G wireless applications," *Int. J. Electr. Comput. Eng. (IJECE)*, vol. 11, no. 3, p. 2238, Jun. 2021.

[10] R. Ullah, S. Ullah, S. M. Umar, R. Ullah, and B. Kamal, "Design and modeling of a 28/38/60/70/80 GHz antenna for fifth generation (5G) mobile and millimeter wave (mmW) applications," in *Proc. Int. Conf. Electr., Commun., Comput. Eng. (ICECCE)*, Jul. 2019, pp. 1–7, doi: 10.1109/ICECCE47252.2019.8940640.

[11] Q. Lv, Y.-H. Yang, S.-G. Zhou, C. Shao, D. Zhou, and C.-Y.-D. Sim, "Design of a single-layer ±45° dual-polarized directional array antenna for millimeter wave applications," *Sensors*, vol. 21, no. 13, p. 4326, Jun. 2021, doi: 10.3390/s21134326.

[12] Y.-H. Yang, S.-G. Zhou, and Y.-L. Dong, "A single-layer ±45° dual-polarized array antenna based on phase control approach," in *Proc. Int. Symp. Antennas Propag. (ISAP)*, Jan. 2021, pp. 245–246.

[13] Y. Zhu, S. Ma, K. Chen, and W. Hong, "A dual-band stacked slotted circular patch antenna for 5G millimeter-wave applications," in *Proc. 8th Int. Conf. Commun. Electron. Syst. (ICCES)*, Jun. 2023, pp. 455–459.

[14] A. Raeesi, A. Palizban, A. Ehsandar, H. Al-Saedi, S. Gigoyan, W. M. Abdel-Wahab, and S. Safavi-Naeini, "A low-profile 2D passive phased-array antenna-in-package for emerging millimeter-wave applications," *IEEE Trans. Antennas Propag.*, vol. 71, no. 1, pp. 1093–1098, Jan. 2023, doi: 10.1109/TAP.2022.3207203.

[15] Y.-H. Yang, B.-H. Sun, G.-X. Zhang, and L. Shen, "TFSIW-excited dual-polarized array antenna with 30° beam-pointing for millimeter-wave applications," *IEEE Trans. Antennas Propag.*, vol. 67, no. 8, pp. 5740–5745, Aug. 2019.

[16] D. D. Devisasi Kala and D. T. Sundari, "A review on optimization of antenna array by evolutionary optimization techniques," *Int. J. Intell. Unmanned Syst.*, vol. 11, no. 1, pp. 151–165, Jan. 2023.

[17] W. Liu, Z. Wang, X. Liu, N. Zeng, Y. Liu, and F. E. Alsaadi, "A survey of deep neural network architectures and their applications," *Neurocomputing*, vol. 234, pp. 11–26, Apr. 2017.

[18] J. H. Kim and S. W. Choi, "A deep learning-based approach for radiation pattern synthesis of an array antenna," *IEEE Access*, vol. 8, pp. 226059–226063, 2020, doi: 10.1109/ACCESS.2020.3045464.

[19] A. M. Montaser and K. R. Mahmoud, "Deep learning based antenna design and beam-steering capabilities for millimeter-wave applications," *IEEE Access*, vol. 9, pp. 145583–145591, 2021, doi: 10.1109/ACCESS.2021.3123219.

[20] A. Zaib, A. R. Masood, M. A. Abdullah, S. Khattak, A. B. Saleem, and I. Ullah, "AESA antennas using machine learning with reduced dataset," *Radioengineering*, vol. 33, no. 3, pp. 397–405, Sep. 2024.

[21] Z. Liang, H. Gao, C. Jin, and J. Deng, "Beam steering for array antenna based on deep learning," in *Proc. Int. Appl. Comput. Electromagn. Soc. Symp. (ACES-China)*, Aug. 2023, pp. 1–2.

[22] X. Yang, D. Yang, Y. Zhao, J. Pan, and Y. Chen, "Synthesis of linear sparse array using DNN-based machine-learning method," *IEEE Trans. Antennas Propag.*, vol. 71, no. 8, pp. 6513–6522, Aug. 2023.

[23] P. Di Barba and Ł. Januszkiewicz, "Linear antenna array modeling with deep neural networks," *Int. J. Appl. Electromagn. Mech.*, vol. 73, no. 4, pp. 303–320, Dec. 2023.

[24] A. Arce, F. Arce, E. Stevens-Navarro, U. Pineda-Rico, M. Cardenas-Juarez, and A. Garcia-Barrientos, "Recurrent deep learning for beam pattern synthesis in optimized antenna arrays," *Appl. Sci.*, vol. 15, no. 1, p. 204, Dec. 2024.

[25] H. Al Kassir, Z. D. Zaharis, P. I. Lazaridis, N. V. Kantartzis, T. V. Yioultsis, I. P. Chochliouros, A. Mihovska, and T. D. Xenos, "Antenna array beamforming based on deep learning neural network architectures," in *Proc. 3rd URSI Atlantic Asia–Pacific Radio Sci. Meeting (AT-AP-RASC)*, May 2022, pp. 1–4.

[26] J. W. Li, Y. Hu, L. Xiang, Z. H. Ma, and W. Hong, "Millimeter wave broadband circularly polarized antenna and array with stacked structure," in *IEEE MTT-S Int. Microw. Symp. Dig.*, May 2021, pp. 1–3.

[27] S. Z. M. Hamzah, N. F. A. Malek, F. N. M. Isa, S. Y. Mohammad, A. W. Azman, and M. R. Islam, "Design of dual-linearly polarized patch antenna at millimetrewaves," in *Proc. IEEE Int. Symp. Antennas Propag. USNC-URSI Radio Sci. Meeting (AP-S/URSI)*, Jul. 2022, pp. 1184–1185, doi: 10.1109/AP-S/USNC-URSI47032.2022.9886499.

[28] T. Rao, R. Pandey, and A. Kandu, "Design a wideband aperture coupled stacked microstrip antenna at 28 GHz for 5G applications," *Int. J. Sci. Prog. Res.*, vol. 74, pp. 61–65, Jun. 2020.

[29] M. Reyad, A. M. Sarhan, and M. Arafa, "A modified Adam algorithm for deep neural network optimization," *Neural Comput. Appl.*, vol. 35, no. 23, pp. 17095–17112, Aug. 2023.

[30] R. J. Erb, "Introduction to backpropagation neural network computation," *Pharm Res.*, vol. 10, no. 2, pp. 165–170, Jan. 1993.

[31] D. M. Pozar, S. D. Targonski, and R. Pokuls, "A shaped-beam microstrip patch reflectarray," *IEEE Trans. Antennas Propag.*, vol. 47, no. 7, pp. 1167–1173, Jul. 1999.

[32] D. M. Pozar, "The active element pattern," *IEEE Trans. Antennas Propag.*, vol. 42, no. 8, pp. 1176–1178, Aug. 1994, doi: 10.1109/8.310010.

[33] Q.-Q. He and B.-Z. Wang, "Design of microstrip array antenna by using active element pattern technique combining with Taylor synthesis method," *Prog. Electromagn. Res.*, vol. 80, pp. 63–76, 2008.

[34] TMYTEK. *BBoard 5G: Beamforming Edu Kit for Mmwave Prototyping, R&D, and 5G Class*. Accessed: Feb. 14, 2025. [Online]. Available: https://tmytek.com/products/beamformers/bboard

[35] (2023). *R2 Product R2 Light Type CATR Meas. System*. Accessed: Feb. 14, 2025. [Online]. Available: https://atenlab.com.tw/en/rclass/r2product/

[36] *Array Factor*. Accessed: Feb. 14, 2025. [Online]. Available: https://www.mathworks.com/help/antenna/ref/lineararray.arrayfactor.html

[37] X. Liu, H. Lu, Y. He, F. Wu, C. Zhang, and X. Wang, "Analysis on the effect of phase noise on the performance of satellite communication and measurement system," *Symmetry*, vol. 15, no. 11, p. 2053, Nov. 2023.

[38] Y. Tsuchiya, N. Suga, K. Uruma, and M. Fujisawa, "Active element arrangement for deep learning-based CSI prediction in IRS-assisted systems," *IEEE Access*, vol. 13, pp. 2829–2843, 2025.

[39] G. Formis, S. Scanzio, L. Wisniewski, and G. Cena, "Mixing neural networks and exponential moving averages for predicting wireless links behavior," in *Proc. IEEE 7th Int. Conf. Ind. Cyber-Physical Syst. (ICPS)*, May 2024, pp. 1–6.

[40] Y. Zhao, L. Xiao, Y. Liu, A. T. Leong, and E. X. Wu, "Electromagnetic interference elimination via active sensing and deep learning prediction for radiofrequency shielding-free MRI," *NMR Biomed.*, vol. 37, no. 7, p. 4956, Jul. 2024.

[41] S.-G. Lee and J.-H. Lee, "Calculating array patterns using an active element pattern method with ground edge effects," *J. Electromagn. Eng. Sci.*, vol. 18, no. 3, pp. 175–181, Jul. 2018.

SITI ZAINAB M. HAMZAH (Member, IEEE) received the B.S. degree in communication engineering from International Islamic University Malaysia, Malaysia, in 2014, and the M.S. degree in electrical engineering from Universiti Tun Hussein Onn Malaysia, in 2018. She is currently pursuing the Ph.D. degree in communication engineering with International Islamic University Malaysia. She is also a Lecturer with Universiti Malaysia Sarawak (UNIMAS). She also did Research Attachment with the Antenna Laboratory, Department of Electronic Engineering, Chang Gung University, in 2023. Her research interests include the development of antenna at high frequency, artificial intelligence and machine learning, neural network processing, and fabrication of antenna. She was a recipient of the IEEE-APS-URSI Student Travel Grant Award, Denver, CO, USA, in 2022.

NORUN FARIHAH ABDUL MALEK (Senior Member, IEEE) received the bachelor's degree (Hons.) in communication engineering from International Islamic University Malaysia (IIUM), Kuala Lumpur, Malaysia, in 2006, and the master's degree in digital communication systems and Ph.D. degree in communication engineering from Loughborough University, in 2007 and 2013, respectively. Later, she was appointed as an Assistant Lecturer with IIUM. She was an Assistant Professor with IIUM, where she is currently an Associate Professor. She did her attachment with Intel Malaysia Sdn. Bhd. under MOHE-Intel Elite Internship Program 2020. She has secured many grants with a total amount of up to MYR500K. Her research interests include antenna and propagation, signal processing, particularly antenna arrays, algorithms, and wireless communication systems. She has been awarded the IEEE Volunteer Award 2021 by the IEEE AP/MTT/EMC Malaysia Joint Chapter Society.

SARAH YASMIN MOHAMAD (Senior Member, IEEE) received the M.Eng. degree in communication and computer engineering from Universiti Kebangsaan Malaysia (UKM), in 2011, and the Ph.D. degree in electrical and electronic engineering from Queen's University Belfast, Northern Ireland, in 2015. She has been an Assistant Professor with the Department of Electrical and Computer Engineering, Faculty of Engineering, International Islamic University Malaysia (IIUM), since 2015. Her research interests include antenna design, analysis and measurement, ground plane architectures for wideband antennas, radar, and wireless communication systems.

FARAH NADIA MOHD ISA (Senior Member, IEEE) received the Ph.D. degree from University College London, in 2013. She is currently a Senior Lecturer with the Department of Electrical and Computer Engineering, International Islamic University Malaysia. She working on the antenna design of a geophysical avalanche radar. She has received numerous scholarships for her academic excellence from Telekom Malaysia, Ministry of Higher Education Malaysia, and UCL. Since returning from her Ph.D., she has been actively involved with the think tank group of creating climate resilient cities in Malaysia an effort from SEADPRI-UKM and NADMA. She is also a Visiting Research Scholar with the Center of Intelligent Antennas and Radio Systems (CIARS), University of Waterloo, Canada. She then re-aligned her focus to help the communities affected by landslides by developing tools to predict the event of landslides as an early warning system. Her current research focused on applying a new generation of radar, software-defined radar to understanding, and predicting landslide susceptibility. She has received RAGS, RIGS, and FRGS (total RM 700,00) grants from the Ministry of Higher Education to help support her current research. She is a member of IET and an Exco Member of the Malaysian Young Scientist Network of the Academy of Sciences Malaysia.

TEDDY SURYA GUNAWAN (Senior Member, IEEE) received the B.Eng. degree (cum laude) in electrical engineering from Institut Teknologi Bandung (ITB), Indonesia, in 1998, the M.Eng. degree from the School of Computer Engineering, Nanyang Technological University, Singapore, in 2001, and the Ph.D. degree from the School of Electrical Engineering and Telecommunications, University of New South Wales, Australia, in 2007. He has been a Professor, since 2019, and was the Head of Department of the Department of Electrical and Computer Engineering, from 2015 to 2016, and the Head of the Program Accreditation and Quality Assurance for the Faculty of Engineering, International Islamic University Malaysia, from 2017 to 2018. His research interests include speech and audio processing, biomedical signal processing and instrumentation, image and video processing, and parallel computing. He has been a Chartered Engineer of IET, U.K., Insinyur Profesional Madya (PII), Indonesia, since 2016, Insinyur Profesional Utama, since 2021, and a registered ASEAN Engineer, since 2018. He was the Chairman of the IEEE Instrumentation and Measurement Society–Malaysia Section, from 2013 to 2014.

KUO-SHENG CHIN (Senior Member, IEEE) received the B.S. degree in electrical engineering from the Chung Cheng Institute of Technology, Taoyuan, Taiwan, in 1986, the M.S.E.E. degree from Syracuse University, Syracuse, NY, USA, in 1993, and the Ph.D. degree in communication engineering from National Chiao Tung University, Hsinchu, Taiwan, in 2005. From 1986 to 2005, he was with the Chung Shan Institute of Science and Technology, Taoyuan, as a Research Assistant, becoming an Assistant Scientist, and then an Associate Scientist. He joined Chang Gung University, Taoyuan, as a Faculty Member, in 2006, where he is currently a Professor with the Department of Electronic Engineering. He supervised a student team to win first place in the 2009 National Electromagnetism Application Innovation Competition, Taiwan. His current research interests include microwave and millimeter-wave couplers, filters, duplexers, low-temperature co-fired ceramic circuits, automotive radar antennas, frequency-selective surfaces, filtering antennas, radomes, and electromagnetic pulse research. He was a recipient of the Best Paper Award of the International Conference on Electromagnetic Near Field Characterization and Imaging, in 2009, the Honorable Paper Award of the International High-Speed Intelligent Communication Forum, in 2010, the Best Student Paper Award of the International Symposium on Next-Generation Electronics, in 2014, the Best Paper Award of the Taiwan Precision Engineering Workshop, in 2016, and the Best Student Paper Award of 2018 the 8th International Symposium on InfoComm and Mechatronics Technology in Bio-Medical and Healthcare Application. He received the Outstanding Teacher Award from Chang Gung University, in 2014 and 2021. He served as an Associate Editor for *Microwave and Optical Technology Letters*, from 2019 to 2020.